Physics in Medicine & Biology

IPEM
Institute of Physics and
Engineering in Medicine

PAPER

Advances in heterostructured scintillators: toward a new generation of detectors for TOF-PET

Fiammetta Pagano[1,2] ⓘ, Nicolaus Kratochwil[1,3] ⓘ, Matteo Salomoni[1], Marco Pizzichemi[1,2], Marco Paganoni[1,2] and Etiennette Auffray[1]

[1] CERN, Esplanade de Particules 1, 1211 Meyrin (Geneva), Switzerland
[2] University of Milano-Bicocca, Piazza dell'Ateneo Nuovo 1, I-20126 Milan, Italy
[3] University of Vienna, Universitaetsring 1, A-1010 Vienna, Austria

E-mail: fiammetta.pagano@cern.ch

Abstract

Objective. Time-of-flight-positron emission tomography would highly benefit from a coincidence time resolution (CTR) below 100 ps: improvement in image quality and patient workflow, and reduction of delivered dose are among them. This achievement proved to be quite challenging, and many approaches have been proposed and are being investigated for this scope. One of the most recent consists in combining different materials with complementary properties (e.g. high stopping power for 511 keV γ-ray and fast timing) in a so-called *heterostructure*, *metascintillator* or *metapixel*. By exploiting a mechanism of energy sharing between the two materials, it is possible to obtain a fraction of fast events which significantly improves the overall time resolution of the system. *Approach.* In this work, we present the progress on this innovative technology. After a simulation study using the Geant4 toolkit, aimed at understanding the optimal configuration in terms of energy sharing, we assembled four heterostructures with alternating plates of BGO and EJ232 plastic scintillator. We fabricated heterostructures of two different sizes ($3 \times 3 \times 3$ mm^3 and $3 \times 3 \times 15$ mm^3), each made up of plates with two different thicknesses of plastic plates. We compared the timing of these pixels with a standard bulk BGO crystal and a structure made of only BGO plates (*layered* BGO). *Main results.* CTR values of 239 ± 12 ps and 197 ± 10 ps FWHM were obtained for the 15 mm long heterostructures with 100 μm and 200 μm thick EJ232 plates (both with 100 μm thick BGO plates), compared to 271 ± 14 ps and 303 ± 15 ps CTR for bulk and layered BGO, respectively. *Significance.* Significant improvements in timing compared to standard bulk BGO were obtained for all the configurations tested. Moreover, for the long pixels, depth of interaction (DOI) collimated measurements were also performed, allowing to validate a simple model describing light transport inside the heterostructure.

1. Introduction

Positron emission tomography (PET) is the best performing medical imaging technique in terms of molecular sensitivity and quantitative accuracy. It allows, for instance, the early diagnosis, staging and follow-up of cancer as well as the diagnosis of some neurodegenerative diseases, like Alzheimer. The main drawbacks of PET are the higher dose delivered to the patient and worse spatial resolution compared to other medical imaging modalities, such as computed tomography (CT) and magnetic resonance imaging (MRI).

Time-of-flight (TOF) technique is one of the most valid ways to further improve the performances of PET. The advantages of TOF-PET have been exhaustively covered in the past by Moses and Derenzo (1999), Conti (2009), Lois *et al* (2010), and Conti (2011). These include: more precise localization of the annihilation point along the line-of-response (LOR), better rejection of random coincidences and better signal-to-noise ratio (SNR). An improved SNR in PET can be exploited in two different ways. By keeping the same acquisition time
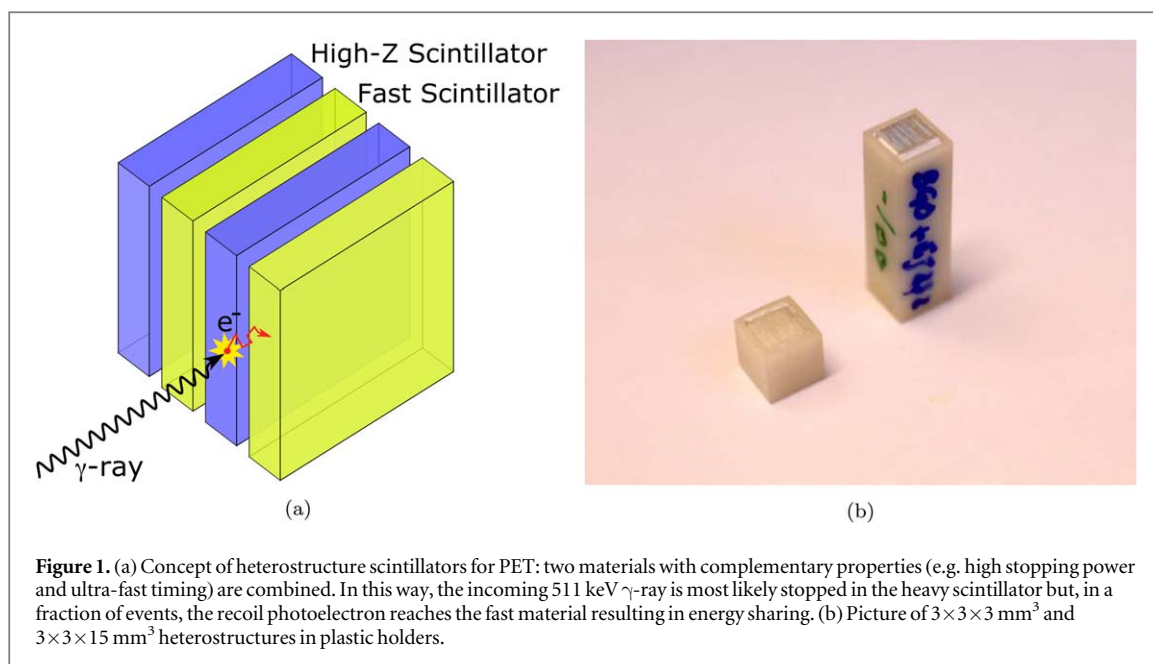
Figure 1. (a) Concept of heterostructure scintillators for PET: two materials with complementary properties (e.g. high stopping power and ultra-fast timing) are combined. In this way, the incoming 511 keV γ-ray is most likely stopped in the heavy scintillator but, in a fraction of events, the recoil photoelectron reaches the fast material resulting in energy sharing. (b) Picture of 3×3×3 mm^3 and 3×3×15 mm^3 heterostructures in plastic holders.

and delivered dose as compared to non-TOF PET, a better image quality can be provided. Otherwise, the same image quality of non-TOF PET scanners can be delivered with either shorter acquisition times, or lower amount of radioactive dose (Conti 2011).

Since the TOF SNR gain is inversely proportional to the time resolution (Moses 2003), the smaller the time resolution, the better the SNR. Already with moderate coincidence time resolution (CTR)—in the order of a few hundreds of picoseconds—the TOF SNR gain is significant: TOF technique is widely used at the clinical level and most of the commercially available PET scanners have a time resolution between 300–500 ps, except for the PET-CT scanner Biograph Vision from Siemens which with 214 ps represents the state-of-the-art (Van Sluis *et al* 2019). However, to have direct effects on the spatial resolution, the CTR must be below 20 ps full width at half maximum (FWHM), since the relation between spatial and time resolution (Δx and Δt, respectively) is given by $\Delta x = \Delta t \cdot c/2$, c being the speed of light in vacuum (Moses 2003).

A challenge has been launched to reach the production of a 10 ps CTR TOF-PET scanner (The 10 ps challenge website 2020, Lecoq *et al* 2020). This level of timing resolution constitutes the ultimate goal because a CTR of 10 ps corresponds to a spatial resolution along the LOR of 1.5 mm, comparable with the range of positron in human tissues, which represents one of the intrinsic limits of PET.

Many lines of research are active in this field, focusing both on the hunt for the most suitable material (Gundacker *et al* 2016, 2020), on the optimization of the photodetector (Nolet *et al* 2018, Gola *et al* 2019) and of the readout electronics (Gundacker *et al* 2019, Gomez *et al* 2021, Pourashraf *et al* 2021, Enoch *et al* 2021). Recent works focusing on the material stage aim to exploit different—and faster—photon emission processes than standard scintillation: e.g. Cherenkov photons (Brunner and Schaart 2017, Arino-Estrada *et al* 2020, Kratochwil *et al* 2021, Terragni *et al* 2022), cross-luminescence (Pots *et al* 2020, Gundacker *et al* 2021, Vaněček *et al* 2021), hot-intraband luminescence (Omelkov *et al* 2016, Turtos *et al* 2019a), and quantum confinement properties of nanocrystals (Tomanova *et al* 2019, Děcka *et al* 2022, Toci *et al* 2019, Perego *et al* 2021). However, all these alternatives show some disadvantages, typically low photon yield or low stopping power for 511 keV γ-ray.

A new approach has been proposed to work around this problem which consists in combining two materials with complementary properties in a so-called *heterostructure*, *metascintillator* or *metapixel* (Turtos *et al* 2019b). The underlying principle to heterostructures is the energy sharing mechanism: when combining a high-Z scintillator with a fast but low-density material, the incoming γ-ray is most likely stopped in the heavy material, but for a fraction of events the recoil photoelectron can deposit energy in both materials—*shared events*—as illustrated in figure 1(a). The more energy is deposited in the fast material, the more fast photons are produced, improving the overall time resolution of the detector.

Recent studies have investigated the possibility to replace plastic scintillators with other materials (Turtos *et al* 2019b, Lecoq 2021, Konstantinou *et al* 2021, Krause *et al* 2021, Děcka *et al* 2022). However, because of the complexity of these structures in terms of light transport and light extraction, the combination of two well-known and easy-to-handle materials such as BGO and plastic scintillators is a good tool to deeply understand and optimize the properties of heterostructures.

For this reason, in this work, we decided to still focus on heterostructures made of alternating layers of BGO and plastic scintillator. The first part of this study consists of a simulation work aimed to find the optimal trade-off between high fraction of energy sharing and a sufficiently good stopping power (section 2.1). Based on simulation results, we chose two different configurations to assemble and experimentally measure the heterostructure (section 2.2). For each of these configurations, two heterostructures (hence a total of four) were built with different size: $3 \times 3 \times 3$ mm^3 and $3 \times 3 \times 15$ mm^3 (figure 1(b)). The results of the measurements are presented and discussed in sections 3 and 4.

2. Methods

2.1. Geant4 simulation

Monte Carlo simulations with the Geant4 toolkit were performed in order to systematically study the variation of key parameters for TOF-PET of heterostructures in comparison to bulk materials. In particular, we focused on the variation of photoelectric probability, the percentage of shared 511 keV events and the mean energy deposited in plastic—which directly affects the number of fast photons produced—as a function of the amount of plastic in the heterostructure.

First, a bulk BGO crystal was simulated to establish the mean distance travelled by a photoelectron of 511 keV events from its emission point. Indeed, because of the interaction mechanism of electrons with matter and the high atomic number of BGO, the CSDA (continuous-slowing-down approximation) range is significantly different from the geometrical distance between the emission and absorption point (projected range). According to the NIST database (Berger *et al* 2017), the CSDA range of an electron of 500 keV in BGO is 2.982×10^{-1} g cm^{-2}, i.e. about 420 μm. From Monte Carlo simulations, the projected range of 511 keV electrons in BGO resulted to be about 70 μm. A recent work by Loignon-Houle *et al* (2022), performed on recoil electrons after photoelectric interaction of 511 keV γ-ray, confirms this value being below 100 μm.

Overall, considering the projected range, the fragility of the crystal plates and the possible implications on the light transport efficiency, the thickness of the BGO plates was selected to be 100 μm. From the study of Loignon-Houle *et al* (2022), it resulted that around 50% of the photoelectrons manage to exceed 100 μm distance from the production point, being potentially able to escape from BGO plates. Keeping fixed also the overall size of the heterostructure ($3 \times 3 \times 3$ mm^3 for the short pixel and $3 \times 3 \times 15$ mm^3 for the long one), the thickness of plates of plastic scintillator has been varied from 10 μm to 220 μm in steps of 10 μm. A 511 keV γ ray source was placed in front of the pixels, shooting in random direction toward the 3×3 mm^2 face, as shown in figure 2. A sample of 500 000 events was used for each configuration.

The focus of these simulations was the energy deposition—how many events deposit 511 keV, how many of these events deposit energy in both materials, and how much energy is deposited in plastic—therefore only the chemical composition, the atomic number, and the density of the two materials were taken into account, while the scintillation and optical properties were neglected.
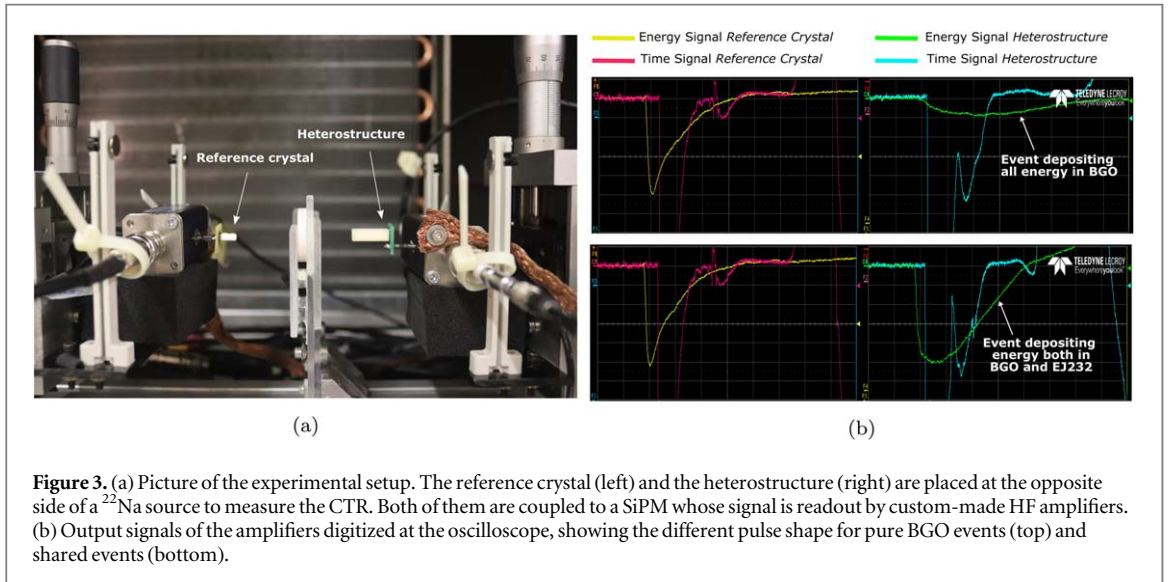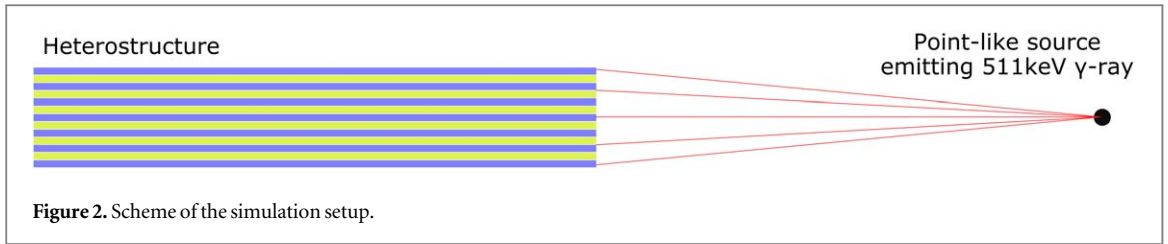
The photoelectric probability was evaluated as the percentage of events depositing more than 400 keV (therefore including the photoelectric events with following X-ray escape) compared to the total of events interacting in the pixel. The percentage of shared 511 keV was calculated as the fraction of photoelectric events depositing at least 50 keV (same threshold applied also in the analysis of the experimental data) in plastic. Finally, for each shared 511 keV event, the amount of energy deposited in plastic was considered and the average over all the events was evaluated.

The simulations were performed also for pure BGO and pure LYSO crystals (both $3 \times 3 \times 3$ mm^3 and $3 \times 3 \times 15$ mm^3). In this case only the photoelectric probability was evaluated, allowing to quantify the sensitivity loss of heterostructure in relation to pure BGO and to compare the sensitivity of heterostructure with LYSO, a standard scintillator for TOF-PET nowadays.

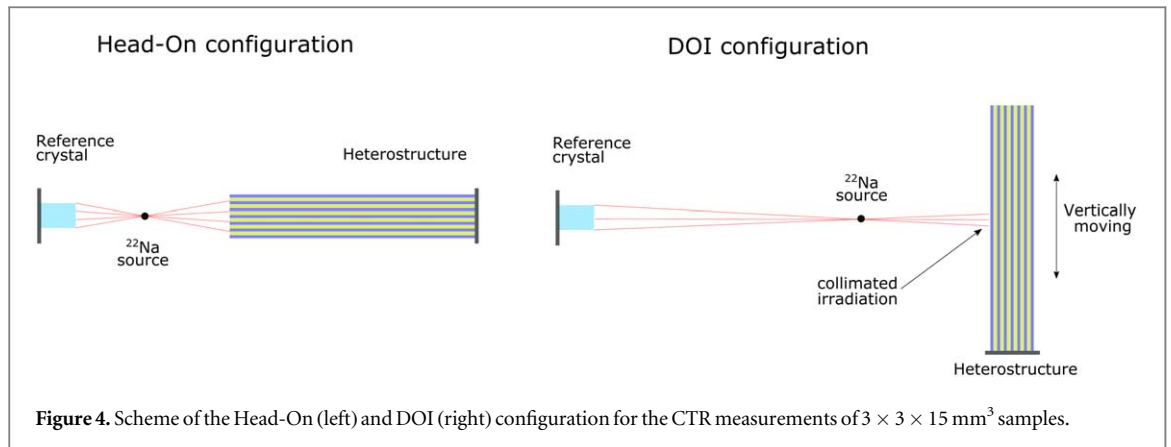### 2.2. CTR measurements

2.2.1. Experimental Setup

To carry out the study on heterostructures for TOF-PET applications, we selected EJ232 from Eljen (Eljen technology EJ232 datasheet) as the fast plastic scintillator to combine with BGO. Compared to BC422 plastic scintillator from Saint Gobain used in previous studies (Turtos *et al* 2019b), EJ232 has similar scintillation properties. Rise- and decay-time were measured to be about 30 ps and below 2 ns respectively, while light yield values of 8000–10 000 ph MeV^{-1} are reported in the data-sheet. On the other hand, EJ232 can more easily be produced in thin plates with polished surfaces, up to 50 μm thickness. Therefore, all the plates used for these heterostructures (both of BGO and plastic) had polished surfaces, except for the edges which could not be polished due to the sub-millimeter size.

Figure 2. Scheme of the simulation setup.

Figure 3. (a) Picture of the experimental setup. The reference crystal (left) and the heterostructure (right) are placed at the opposite side of a ^{22}Na source to measure the CTR. Both of them are coupled to a SiPM whose signal is readout by custom-made HF amplifiers. (b) Output signals of the amplifiers digitized at the oscilloscope, showing the different pulse shape for pure BGO events (top) and shared events (bottom).

Four different heterostructured pixels were assembled in our workshop at CERN: two different thicknesses for plastic plates were chosen taking into account the simulation results, and for each of them both short ($3 \times 3 \times 3$ mm^3) and long ($3 \times 3 \times 15$ mm^3) pixels were built. As it is shown in section 3.1, when both plastic and BGO plates have a thickness of 100 μm, the photoelectric probability of the heterostructure is comparable to the one of a LYSO crystal of same size, and the mean energy deposited in plastic is about one third of the total. We therefore chose this working condition as optimal, since it provides similar stopping power to the standard material used nowadays in PET scanners, i.e. LYSO, while introducing a ultra-fast scintillation component. Subsequently, a further configuration with 200 μm thick plastic plates was tested, in order to explore the timing limits of this kind of structures. From now on, the two configurations will be referred to as *100–100* and *100–200* configuration respectively.

For each sample, the CTR was measured with the experimental setup shown in figure 3(a). The heterostructure was measured in coincidence with a reference crystal ($2 \times 2 \times 3$ mm^3 LSO:Ce:0.4%Ca, CTR $= 61 \pm 3$ ps FWHM), placed at the opposite side of a ^{22}Na source. Both the reference crystal and the heterostructure were coupled to SiPMs with Cargille Meltmount glue (refractive index $n = 1.58$). For the heterostructures, a 3.7×3.7 mm^2 Broadcom SiPM 30 μm SPAD size (AFBR-S4N44C013), biased with an overvoltage of about 11 V, was used. This type of SiPM provides excellent detection efficiency for both EJ232 and BGO emission as well as intrinsic single photon time resolution of 88 ± 6 ps FWHM (Gundacker *et al* 2020). The SiPM signal is read out by a custom made amplifier which splits the signal in two, in order to independently optimize the energy (analog amplifier) and time (high-frequency amplifier (Cates *et al* 2018)) information. The output signals are finally digitized by a LeCroy DDA735Zi oscilloscope (3.5 GHz bandwidth, 20 Gs s^{-1} sample rate), as shown in figure 3(b). A more detailed description of the bench and in particular of the high-frequency electronics was previously reported by Gundacker *et al* (2019).

Both short and long pixels were measured in *head-on configuration*, with the opposite surface to the SiPM of the reference crystal and of the heterostructure facing each other (as shown in the left side of figure 4). Only the long pixels were measured also in *DOI* (depth of interaction) *configuration*: the reference detector and the heterostructure were placed at a distance of 80 mm, with the source 10 mm away from the heterostructure and the latter rotated by 90° compared to the head on configuration (right side of figure 4). By moving the heterostructure along the vertical direction it was possible to perform collimated irradiations in five different spots along the DOI coordinate, separated by 3.5 mm.

Figure 4. Scheme of the Head-On (left) and DOI (right) configuration for the CTR measurements of $3 \times 3 \times 15 \, \text{mm}^3$ samples.

Similar measurements were repeated also for a $3 \times 3 \times 15 \, \text{mm}^3$ bulk BGO crystal and a $3 \times 3 \times 15 \, \text{mm}^3$ layered BGO pixel (i.e. a stack of BGO plates with 100 μm thickness), to validate the improvement of the heterostructure approach.

2.2.2. Data recording
All the necessary information for the analysis was directly extrapolated from the waveforms at the oscilloscope. The energy signal of both left and right channels (reference crystal and heterostructure respectively) were integrated over 160 ns to select offline the photopeak events. For the right channel also the signal amplitude was acquired. In this way, it was possible to distinguish the events depositing energy in only one or both the two materials via pulse shape discrimination. Indeed, BGO and EJ232 plastic scintillator have different photon time density (similar intrinsic light yield but the decay-time of BGO is about 150 times greater than the one of EJ232), which results in different pulse shape as shown in figure 3(b). Regarding the time signal, a leading-edge threshold was set at the oscilloscope (below the signal amplitude of a single SPAD, which for $3.7 \times 3.7 \, \text{mm}^2$ Broadcom SiPM is 30 mV at 11 V overvoltage) for both the left and right channel, and the coincidence time-delay between the two was calculated. For the time signal of the right channel also the rise-time was measured as the time difference between the crossing of two fixed thresholds. This information was used to correct for the time walk effect.

2.2.3. Data analysis
The first step of the data analysis consists of the selection of photopeak events in both detector arms. However, for heterostructures, given the different scintillation response of the two materials, the selection of events within the energy window of choice can not be done as straightforward as for bulk materials (cutting on the integrated charge, which is proportional to the deposited energy). For this reason, the relation between charge and amplitude was considered. Indeed, as already proved by Turtos *et al* (2019b), this allows to classify the events depositing energy only in BGO, only in plastic, or in both materials. This concept is illustrated in figure 5(a). A coordinates transformation was applied, to pass from the (*amplitude* [V], *charge* [nWb]) to the (*energy in plastic* [keV], *energy in BGO* [keV]) coordinate system. In this way, it was possible to establish for each event the energy deposited in BGO and in plastic (see figure 5(b)), and the 511 keV events were selected as those depositing total energy (sum of the energy deposited in the two materials) between 440 keV and 665 keV. This energy window was set to allow for good statistics and according to clinical TOF-PET scanner (Surti *et al* 2007). Different energy windows were also tested (up to 40 keV both narrower and larger) but without any significant effect on timing. Finally, the 511 keV events depositing at least 50 keV in plastic were classified as *shared* 511 keV events. The threshold was set at 50 keV to ensure the selection of events with an amount of energy deposited in the fast material sufficient to impact the overall timing. On the other hand, by moving this cut at higher values (e.g. 70 keV), the improvement in timing was negligible.

A time walk correction was applied to the selected events, based on the rise time (detailed explanation in Kratochwil *et al* (2020)). The corrected time-delay distribution was considered for both *all* 511 keV and only *shared* 511 keV events and fitted with the sum of two Gaussian functions. The CTR, assuming two identical heterostructures in coincidence, was finally evaluated as the FWHM of the fit curve corrected for the contribution of the reference, e.g. a measured 146 ps FWHM corresponds to $\sqrt{2 \cdot 146^2 - 61^2} = 197 \text{ps CTR}$.
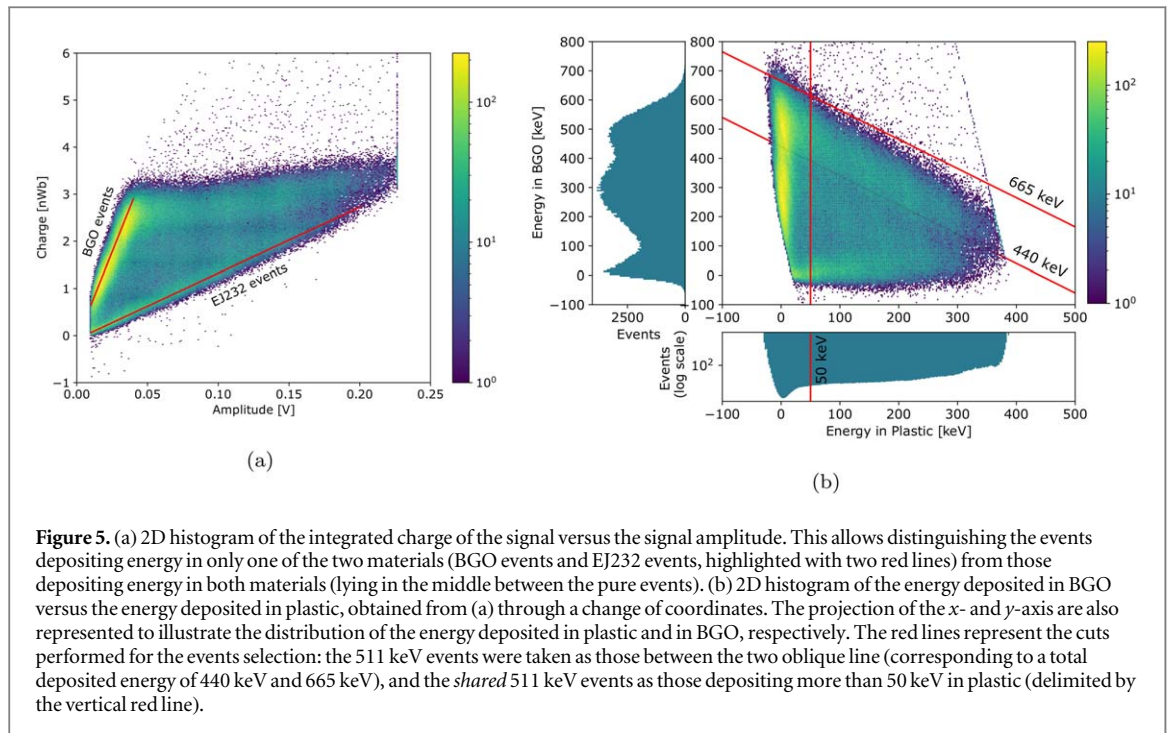
Figure 5. (a) 2D histogram of the integrated charge of the signal versus the signal amplitude. This allows distinguishing the events depositing energy in only one of the two materials (BGO events and EJ232 events, highlighted with two red lines) from those depositing energy in both materials (lying in the middle between the pure events). (b) 2D histogram of the energy deposited in BGO versus the energy deposited in plastic, obtained from (a) through a change of coordinates. The projection of the *x*- and *y*-axis are also represented to illustrate the distribution of the energy deposited in plastic and in BGO, respectively. The red lines represent the cuts performed for the events selection: the 511 keV events were taken as those between the two oblique line (corresponding to a total deposited energy of 440 keV and 665 keV), and the *shared* 511 keV events as those depositing more than 50 keV in plastic (delimited by the vertical red line).

3. Results

3.1. Simulation

The results of the scan over different thicknesses of plastic plates for photoelectric probability, percentage of shared events, and mean deposited energy in plastic are illustrated in figure 6, for both short (left) and long (right) heterostructures. It should be reminded that the following results refer to a single detector.

The photoelectric probability of pure BGO and LYSO of the same dimensions are also represented. The comparison with bulk BGO allows to quantify the sensitivity loss, which goes from 4 % to 37 % for the two extreme thicknesses considered (10 μm and 220 μm, corresponding to the conditions in which, out of the total volume, a fraction of 9 % and 67 % is made of plastic, respectively).

The photoelectric probability of LYSO crystal was instead used as criterion to choose the optimal geometry for this kind of heterostructures. Indeed, L(Y)SO is the state-of-the-art crystal detector for TOF-PET due to its relatively fast decay-time, high stopping power and good energy resolution; however, its photoelectric probability is significantly lower than bulk BGO. From figure 6, it can be seen that for plastic thickness up to 70 μm, the photoelectric probability of the heterostructure is higher than LYSO.

Increasing the plastic thickness in the range of interest, the mean energy deposited in plastic increases from 70 keV to almost 200 keV, and the probability to have shared 511 keV events from 5 % to 65 %.

In particular, looking at the configuration with 100 μm thick plastic plates (and 100 μm thick BGO plates, so half volume plastic and half volume BGO), we see that: the photoelectric probability of the heterostructure is similar to that of an equivalent bulk crystal of LYSO, almost half of the photoelectric events are shared and, for these events, on average one third of the total energy is deposited in plastic.

It must be noted that what changes between the $3 \times 3 \times 3$ mm^3 and $3 \times 3 \times 15$ mm^3 is only the photoelectric probability since the stopping power increases with the pixel length. While the fraction of shared 511 keV, the fraction of energy deposited in plastic and percentage volume of plastic in the heterostructure for which the photoelectric probability is equal to LYSO do not depend on the pixel length.

3.2. CTR results

In table 1, the CTR results of all the samples measured in head-on configuration are summarized. The first thing to notice is the degradation of CTR when passing from a bulk (271 $\pm$ 14 ps) to a layered structure (stack of plates of 100 μm thick plates) with only BGO (303 $\pm$ 15 ps). However, looking at the CTR obtained with the two long heterostructures, it can be observed that a significant improvement in the CTR is registered with respect to bulk BGO, even without distinguishing between all and shared 511 keV. If this distinction is applied, and only the shared 511 keV are considered, the improvement is even greater: 214 $\pm$ 11 ps and 173 $\pm$ 9 ps for the 100–100 and the 100–200 heterostructures respectively, against the 271 $\pm$ 14 ps of bulk BGO and 303 $\pm$ 15 ps of layered BGO.
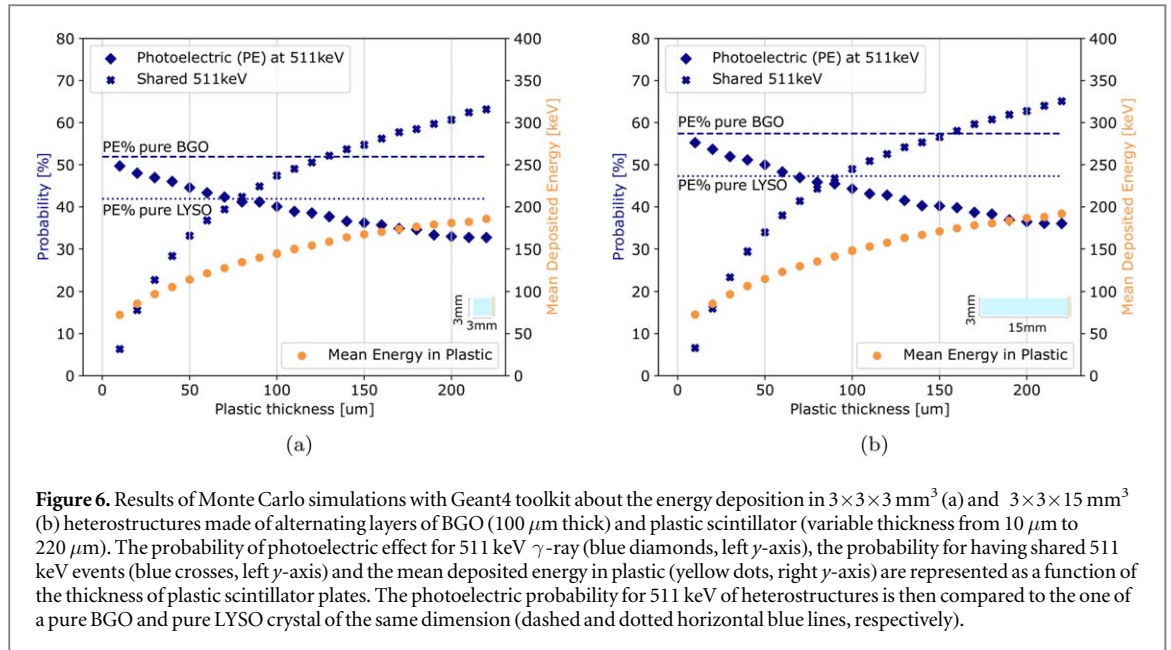
Figure 6. Results of Monte Carlo simulations with Geant4 toolkit about the energy deposition in $3\times3\times3$ mm^3 (a) and $3\times3\times15$ mm^3 (b) heterostructures made of alternating layers of BGO (100 μm thick) and plastic scintillator (variable thickness from 10 μm to 220 μm). The probability of photoelectric effect for 511 keV γ-ray (blue diamonds, left *y*-axis), the probability for having shared 511 keV events (blue crosses, left *y*-axis) and the mean deposited energy in plastic (yellow dots, right *y*-axis) are represented as a function of the thickness of plastic scintillator plates. The photoelectric probability for 511 keV of heterostructures is then compared to the one of a pure BGO and pure LYSO crystal of the same dimension (dashed and dotted horizontal blue lines, respectively).

Table 1. CTR results of all the samples measured in head-on configuration: short ($3\times3\times3$ mm^3) and long ($3\times3\times15$ mm^3) heterostructure with 100 μm thick plastic plates, with 200 μm thick plastic plates, long bulk and layered BGO. For the heterostructures the CTR of both *all* 511 keV and *shared* 511 keV is reported. For both the heterostructure and layered BGO the thickness of BGO plates was 100 μm.

|	100 µm EJ232		200 µm EJ232		bulk BGO	layered BGO
	short	long	short	long	long	long
CTR [ps] All 511 keV	155 ± 8	239 ± 12	142 ± 7	197 ± 10	271 ± 14	303 ± 15
CTR [ps] Shared 511keV	126 ± 6	214 ± 11	114 ± 6	173 ± 9	//	//

In figure 7 the CTR results of both head-on and DOI configurations of the two long heterostructures are illustrated, distinguishing between *all* (figure 7(a)) and only *shared* (figure 7(b)) 511 keV events. The CTR in head-on configuration for bulk and layered BGO are added as comparison.

The trend of CTR as a function of DOI (see figure 7) was already observed also for bulk material by Loignon-Houle *et al* (2021). This can be explained by considering the most relevant effects that contribute to CTR. First of all the light output: the closer the DOI is to the SiPM, the greater is the light output; if this was the only contribution we should expect a monotonic improvement of CTR getting closer to the SiPM since CTR scales inversely with the square root of light output—$CTR \propto 1/\sqrt{\text{LightOutput}}$. However, this is not the case: another important effect that must be considered in view of the fast electronics used, is the photon time spread (PTS). In a $3 \times 3 \times 15$ mm^3 pixel, the first scintillation photons reaching the extraction face are those emitted mainly in two directions: directly toward the SiPM (*direct photons*) or in the opposite direction and then reflected toward the SiPM (*reflected photons*). The distinction between these two categories was first observed in simulation studies (Gundacker *et al* 2013, Cates *et al* 2015), and then also in experimental works (Kratochwil *et al* 2021, Terragni *et al* 2022). For interactions far away from the SiPM, the two categories of photons reach the photodetector at the same time. While for DOI closer to the SiPM, because of the increasing difference in the distance travelled by direct and reflected photons, the variance in the arrival times of optical photons increases, leading to a worsening of the CTR. The sum of the two effects explain why the worse CTR values are obtained for interaction in the central part of the pixels.

The worse CTR for long heterostructures compared to the short ones (see table 1) was expected because of the increasing importance of light transport effects with the increasing pixel length. This effect was quantified using the information coming from DOI measurements, in particular the shift of the time delay peak according to the irradiated DOI (see figure 8(a)). The DOI blurring along the pixel was approximated as the shift of the time
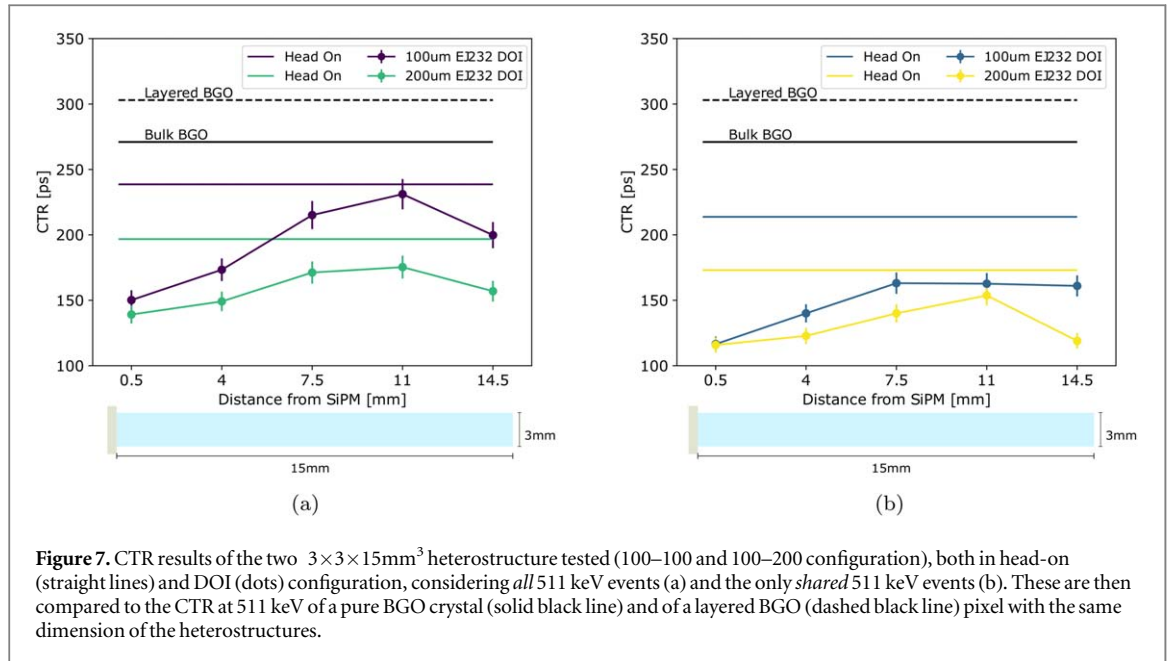
Figure 7. CTR results of the two $3\times3\times15\,mm^3$ heterostructure tested (100–100 and 100–200 configuration), both in head-on (straight lines) and DOI (dots) configuration, considering *all* 511 keV events (a) and the only *shared* 511 keV events (b). These are then compared to the CTR at 511 keV of a pure BGO crystal (solid black line) and of a layered BGO (dashed black line) pixel with the same dimension of the heterostructures.
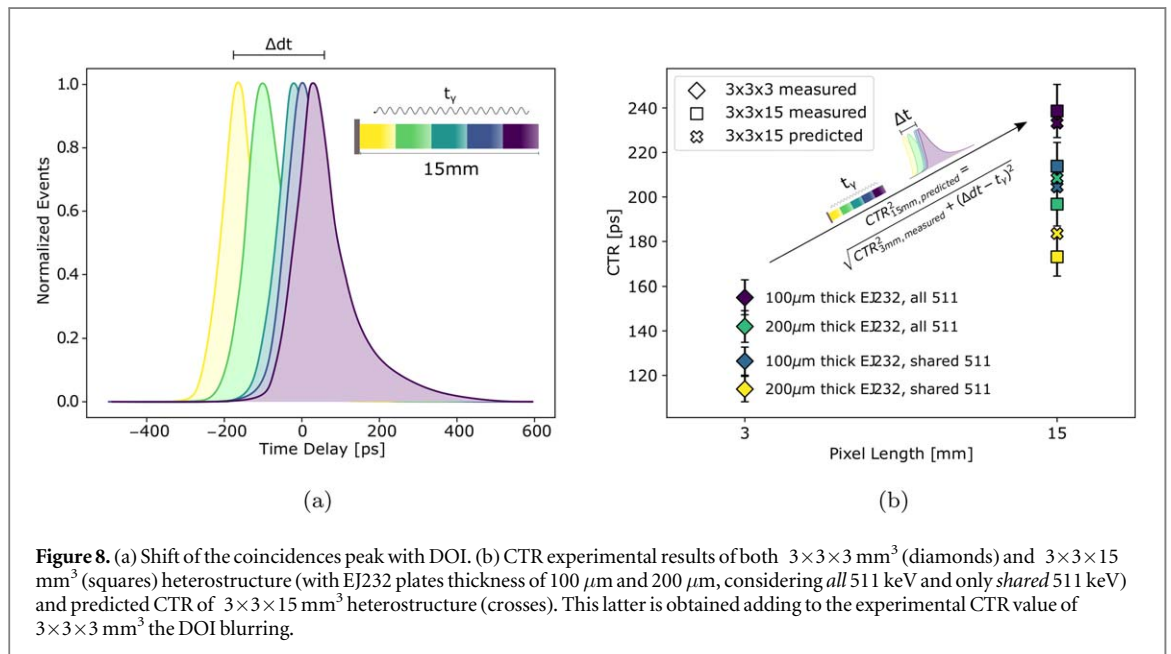
Figure 8. (a) Shift of the coincidences peak with DOI. (b) CTR experimental results of both $3\times3\times3\,mm^3$ (diamonds) and $3\times3\times15\,mm^3$ (squares) heterostructure (with EJ232 plates thickness of 100 μm and 200 μm, considering *all* 511 keV and only *shared* 511 keV) and predicted CTR of $3\times3\times15\,mm^3$ heterostructure (crosses). This latter is obtained adding to the experimental CTR value of $3\times3\times3\,mm^3$ the DOI blurring.

delay peak from the first to the last DOI (Δdt) minus the time that the γ-ray takes to go from the first to the last DOI (t_γ). Both these concepts are illustrated in figure 8(a). By adding in quadrature this contribution to the CTR of the $3 \times 3 \times 3\,mm^3$ pixel (which is comparable with the CTR of the closest DOI to the SiPM of long pixels for both configurations),

$$CTR_{15mm,predicted} = \sqrt{CTR_{3mm,measured}^2 + (\Delta dt - t_\gamma)^2}, \qquad (1)$$

it was possible to obtain the predicted CTR values for the $3 \times 3 \times 15\,mm^3$ pixels. These values resulted in good agreement with the experimental ones, as shown in figure 8(b).

4. Discussion

The improvement in time resolution of heterostructures compared to pure BGO sample of same dimension resulted to be significant: 239 ± 12 ps and 197 ± 10 ps CTR values were obtained with the 100–100 and the 100–200 configuration respectively, instead of 271 ± 14 ps for bulk BGO and 303 ± 15 ps for the layered BGO. The worse CTR of layered BGO compared to bulk BGO is due to the worse light transport in such stratified
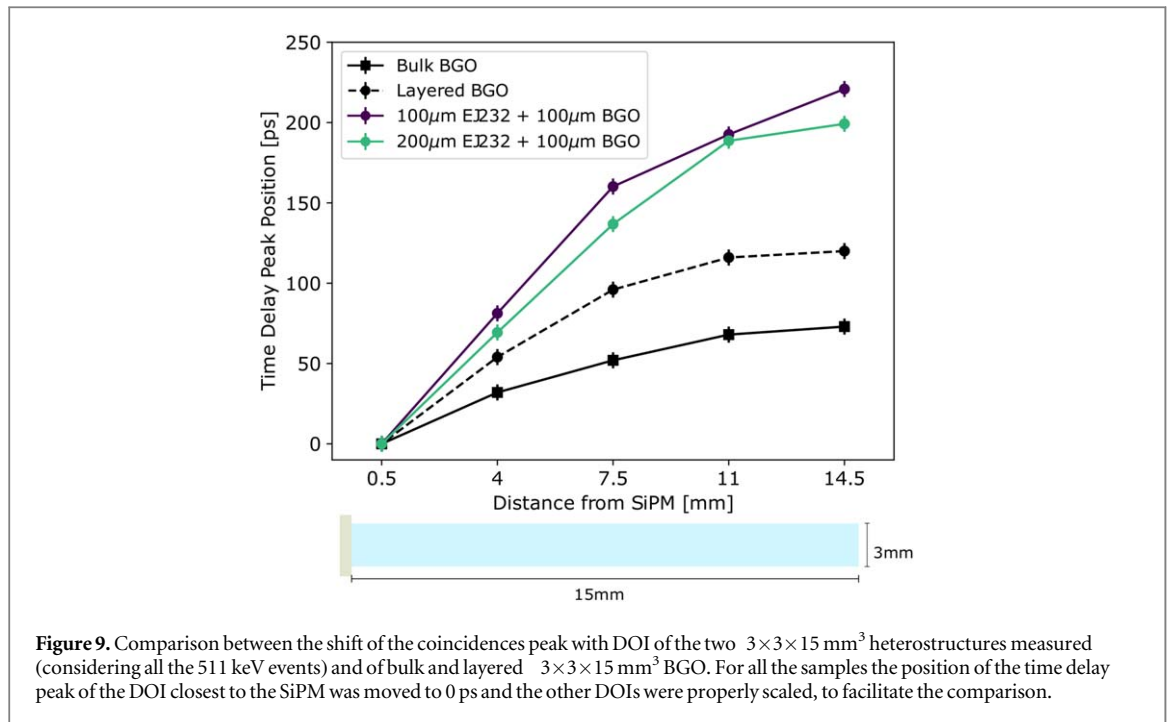
Figure 9. Comparison between the shift of the coincidences peak with DOI of the two $3\times3\times15$ mm^3 heterostructures measured (considering all the 511 keV events) and of bulk and layered $3\times3\times15$ mm^3 BGO. For all the samples the position of the time delay peak of the DOI closest to the SiPM was moved to 0 ps and the other DOIs were properly scaled, to facilitate the comparison.

structures. Taking this into account, the CTR improvement of heterostructures is even more significant: the energy sharing mechanism is effective enough to compensate the degradation introduced by the stratification and to improve the CTR of 12 % and 28 % compared to bulk BGO with the 100–100 and 100–200 configuration respectively, if all photopeak events (depositing energy between 440 keV and 665 keV) are considered. Furthermore, if only the shared events (depositing at least 50 keV in plastic) are selected, the CTR improves of 21 % and of 37 % with the 100–100 and 100–200 configuration respectively, compared to bulk BGO. The distinction in *shared* and *not shared* events can be particularly useful in the reconstruction process: a multi-kernel approach has been proposed by Efthimiou *et al* (2020) and Kratochwil *et al* (2020) to take full advantage of Cherenkov photons of BGO and a similar approach has been already applied also to BGO and plastic heterostructures by Mohr *et al* (2022), just with the purpose to exploit the fast timing of shared events.

A first understanding and estimation of light transport in heterostructures was possible thanks to DOI measurements of long pixels as explained in the previous section and illustrated in figure 8. The good agreement between the measured and expected CTR of long pixels—obtained as shown in equation (1)—confirms that the DOI blurring is one of the main factors related to light transport which contributes to CTR degradation. This also means that equation (1) is a good enough approximation to take into account this effect, and that the shift of the time delay peak is a valid quantity with which estimate the DOI blurring. For this reason, we compared the shift of the coincidences peak among all the $3 \times 3 \times 15$ mm^3 samples measured (heterostructures with 100 μm and 200 μm thick plastic plates, bulk BGO and layered BGO). The results, illustrated in figure 9, show that the shift for the two heterostructures is about three times the shift of bulk BGO and twice the one of layered BGO. This means that also without mixing two materials, but simply passing from bulk to such layered structure, the light transport deteriorates, which actually reflects in worse CTR as shown in table 1. Introducing a different material, with different optical properties, further amplifies the effect. This suggests that one aspect on which it is worth focusing for improving this technology is the optimization of the interface between the two materials. This could be done either using two materials with optical properties as similar as possible or introducing a coupling medium between the layers. Monte Carlo simulations with Geant4 toolkit will be performed in order to investigate thoroughly light transport and how to improve it. However, what can be already deduced from our simplified model (see equation (1)), is that with a material with the same timing properties of EJ232 plastic scintillator but the same DOI effect as in layered BGO, a CTR of 195 ps—instead of 239 ± 12 ps—would be reachable with the 100–100 configuration.

From figure 9 it can be noted that the PTS effect due to DOI blurring is greater for the 100–100 configuration than in the 100–200 one, and this can be explained by considering that in the former there is a higher number of layers. This means that the better CTR of the 100–200 configuration is not only due to the higher number of fast photons produced but also to better light transport. Indeed, the calculation above shows that the difference in CTR between the 100–100 and 100–200 configuration would be less significant (195 ps versus 187 ps, respectively, instead of 239 ps versus 197 ps) if the shift of the coincidences peak of the heterostructure would be

the same of layered BGO. Therefore, improving light transport would allow to significantly improve timing and at the same time to keep a reasonable sensitivity.

High photo-fraction and detection efficiency are indeed mandatory requirements for a TOF-PET module and a possible solution consists of increasing the pixel length, beyond the standard one currently used in TOF-PET scanner of about 20 mm (Van Sluis *et al* 2019, Rausch *et al* 2019) as proposed by Lecoq (2021). However, the longer the crystal length, the stronger the PTS effect, and timing resolution would be affected. For PET scanners based on bulk, standard scintillator (BGO and L(Y)SO), longer crystal shown to be more favorable from a image quality standpoint, since the loss in timing performances is to large extent overcompensated by better detection efficiency. A figure of merit allowing for a trade-off between these two factors is given by Schaart (2021) and Kratochwil *et al* (2020). However, light transport in such layered structures is significantly different from bulk crystals, therefore a different balancing between these two factors can be expected as well. Moreover, longer pixels would contribute to deteriorate the energy resolution, another key parameter for PET which need to be studied further for heterostructures. Indeed, mixing two materials with different scintillation properties could reflect in a degradation of energy resolution. In this work we did not focus on the optimization of the energy resolution since our priority was to demonstrate the gain achievable in timing with BGO-based heterostructures compared to bulk BGO. Future works, starting from the optimization of light transport through Monte Carlo simulations and dedicated experimental studies, will focus on this topic.

Another option to increase the sensitivity of heterostructures is represented by the substitution of plastic by denser and/or even faster material. BaF_2 could represents a good candidate (as also shown by Krause *et al* (2021) and Lecoq (2021)) since its density is almost five times the one of plastic and has a sub-nanosecond decay component. However, its VUV emission makes the light extraction and the photodection more complicate. Another promising alternative which has emerged in the recent years is represented by nanomaterials. Indeed, because of quantum confinement, these materials can show extraordinary fast emission timing and high light output, however their size and generally low stopping power prevent from using them as stand alone detector. Heterostructures represents therefore a great solution to take full advantage of their extraordinary properties. Within the Crystal Clear Collaboration there is already an active line of research focusing on the development of ultra-fast materials based on nanotechnologies (Hospodkova *et al* 2014, Perego *et al* 2021, Děcka *et al* 2022).

Finally, a further aspect that can be optimized is the readout electronics. In parallel with the tuning of light transport through a proper matching of the optical properties of the two material and of the interface between them, the PTS effect can be mitigated correcting for the DOI resolution, which can be obtained either with side readout (Lee *et al* 2021), double sided readout, or utilizing light sharing mechanism in an array (Pizzichemi *et al* 2019).

Overall, heterostructures demonstrated to have good potential for improving the time resolution of standard scintillators while keeping reasonable sensitivity. It should be mentioned that this work is part of the fundamental research toward the goal of reaching 10 ps CTR, but for heterostructures to become competitive with the state-of-the-art TOF-PET scintillators (e.g. L(Y)SO) and to be integrated into a full TOF-PET scanner, there is still a long way to go. Our next step in this direction will be to demonstrate the feasibility of this approach with a matrix of 3 × 3 or 4 × 4 heterostructures coupled to an array of as many SiPM. However, all aspects discussed above—e.g. detection efficiency, energy resolution, light transport, and electronics—need to be optimized from an image quality standpoint to scale from the single-pixel detector to a full TOF-PET scanner. Moreover, different geometries more suitable for large-scale production—such as alternating fibers, drilled holes in the inorganic material filled with a fast material, fibers of inorganic material introduced in the fast material during its production—may also be investigated to simplify this scaling up. However, pixels with alternated plates of BGO and plastic constitute the simplest and most practical tool for carrying on fundamental research on this topic experimentally.

5. Conclusion

In this work, we confirm the potential of heterostructures for TOF-PET application. We focused on heterostructures made of alternating plates of BGO and plastic scintillator. Making use of Monte Carlo simulations, the sensitivity loss and the energy sharing were systematically quantified as a function of the thickness of plastic layers, while the thickness of BGO plates was fixed according to the projected range of a 511 keV electron in it. We chose as an optimal compromise between sensitivity loss and gain in timing the configuration with 100 μm thick plates of both BGO and plastic. For the experimental characterization of BGO and plastic heterostructure, the EJ232 plastic scintillator was used. Four different pixels were assembled: two of size 3 × 3 × 3 mm^3 and 3 × 3 × 15 mm^3 with the optimal configuration (100–100) and other two with a double thickness of EJ232 plates (100–200), in order to investigate the achievable gain in timing with this kind of structure - neglecting the issue regarding sensitivity. A bulk BGO crystal and a layered BGO (stack of 100 μm

thick plates of BGO) of size $3 \times 3 \times 15 \, \text{mm}^3$ were measured in the same conditions as a reference for the CTR of the heterostructures.

Comparing the CTR of both the heterostructures with the two BGO reference samples, a significant improvement was observed: for standard bulk BGO a CTR of 271 ± 14 ps was measured, worsening to 303 ± 15 ps by switching to a layered BGO, but when the fast EJ232 is introduced in this structure, the CTR improves up to 239 ± 12 ps (100 μm EJ232) and 197 ± 10 ps (200 μm EJ232).

By performing DOI collimated measurements, it was possible to link the CTR of the short and long pixels, by means of a simplified model which takes into account the shift of the coincidences peak according to the DOI. This allowed us to identify the proper quantity with which to estimate the PTS, a key limiting factor in the achievable CTR.

Follow-up studies are foreseen to further improve the performances of this novel technology for TOF-PET applications. First of all, a Monte Carlo simulation study focused on optical photons propagation to better understand and improve the light transport. This study will also constitute a starting point for the optimization of the energy resolution of heterostructure. The realization of an array of heterostructures interfacing with a light guide, the side readout, and the double sided readout are all methods that will be evaluated in order to compensate for the DOI blurring and further improve the time resolution. Once all these factors will be optimized, the focus will be moved on the hunting for the most suitable materials to combine in heterostructures.

Acknowledgments

ORCID iDs

Fiammetta Pagano ⓘ https://orcid.org/0000-0001-9938-6799
Nicolaus Kratochwil ⓘ https://orcid.org/0000-0001-5297-1878

References

Ariño-Estrada G, Roncali E, Selfridge A R, Du J, Glodo J, Shah K S and Cherry S R 2020 Study of Cherenkov light emission in the semiconductors TlBr and TlCl for TOF-PET *IEEE Transactions on Radiation and Plasma Medical Sciences* **5** 630–7

Berger M, Coursey J, Zucker M and Chang J 2017 Nist standard reference database 124 - stopping-power & range tables for electrons, protons, and helium ions (https://doi.org/10.18434/T4NC7P)

Brunner S and Schaart D 2017 BGO as a hybrid scintillator/Cherenkov radiator for cost-effective time-of-flight PET *Physics in Medicine & Biology* **62** 4421

Cates J W, Gundacker S, Auffray E, Lecoq P and Levin C S 2018 Improved single photon time resolution for analog SiPMs with front end readout that reduces influence of electronic noise *Physics in Medicine & Biology* **63** 185022

Cates J W, Vinke R and Levin C S 2015 Analytical calculation of the lower bound on timing resolution for PET scintillation detectors comprising high-aspect-ratio crystal elements *Physics in Medicine & Biology* **60** 5141

Conti M 2009 State of the art and challenges of time-of-flight PET *Phys. Med.* **25** 1–11

Conti M 2011 Focus on time-of-flight PET: the benefits of improved time resolution *Eur. J. Nucl. Med. Mol. Imaging* **38** 1147–57

Děcka K, Kral J, Hajek F, Průša P, Babin V, Mihokova E and Čuba V 2022 Scintillation response enhancement in nanocrystalline lead halide perovskite thin films on scintillating wafers *Nanomaterials* **12** 14

Efthimiou N, Kratochwil N, Gundacker S, Polesel A, Salomoni M, Auffray E and Pizzichemi M 2020 TOF-PET image reconstruction with multiple timing kernels applied on Cherenkov radiation in BGO *IEEE transactions on radiation and plasma medical sciences* **5** 703–11

Eljen technology ej232 datasheet (https://eljentechnology.com/products/plasticscintillators/ej-232-ej-232q)

Enoch S, Gola A, Lecoq P and Rivetti A 2021 Design considerations for a new generation of SiPMs with unprecedented timing resolution *J. Instrum.* **16** P02019

Gola A, Acerbi F, Capasso M, Marcante M, Mazzi A, Paternoster G, Piemonte C, Regazzoni V and Zorzi N 2019 NUV-sensitive silicon photomultiplier technologies developed at Fondazione Bruno Kessler *Sensors* **19** 308

Gómez S *et al* 2021 FastIC: a fast integrated circuit for the readout of high performance detectors *J. Instrum.* **17** C05027

Gundacker S, Auffray E, Frisch B, Jarron P, Knapitsch A, Meyer T, Pizzichemi M and Lecoq P 2013 Time of flight positron emission tomography towards 100ps resolution with L(Y)SO: an experimental and theoretical analysis *J. Instrum.* **8** P07014

Gundacker S, Auffray E, Pauwels K and Lecoq P 2016 Measurement of intrinsic rise times for various L (Y) SO and LuAG scintillators with a general study of prompt photons to achieve 10 ps in TOF-PET} *Phys. Med. Biol.* **61** 2802

Gundacker S, Pots R, Nepomnyashchikh A, Radzhabov E, Shendrik R, Omelkov S, Kirm M, Acerbi F, Capasso M and Paternoster G 2021 VUV-SiPMs applied to BaF 2 cross-luminescence detection for high-rate ultrafast timing applications *Phys. Med. Biol.* **66** 114002

Gundacker S, Turtos R M, Auffray E, Paganoni M and Lecoq P 2019 High-frequency SiPM readout advances measured coincidence time resolution limits in TOF-PET *Phys. Med. Biol.* **64** 055012

Gundacker S, Turtos R M, Kratochwil N, Pots R H, Paganoni M, Lecoq P and Auffray E 2020 Experimental time resolution limits of modern SiPMs and TOF-PET detectors exploring different scintillators and Cherenkov emission *Phys. Med. Biol.* **65** 025001

Hospodkova A, Nikl M, Pacherova O, Oswald J, Brůža P, Panek D, Foltynski B, Hulicius E, Beitlerova A and Heuken M 2014 InGaN/GaN multiple quantum well for fast scintillation application: radioluminescence and photoluminescence study *Nanotechnology* **25** 455501

Konstantinou G, Lecoq P, Benlloch J and Gonzalez A 2021 Metascintillators for ultra-fast gamma detectors: A review of current state and future perspectives *IEEE Trans on Radiation and Plasma Medical Sciences* **6** 510–6

Kratochwil N, Auffray E and Gundacker S 2020 Exploring Cherenkov emission of BGO for TOF-PET *IEEE Transactions on Radiation and Plasma Medical Sciences* **5** 619–29

Kratochwil N, Gundacker S and Auffray E 2021 A roadmap for sole Cherenkov radiators with SiPMs in TOF-PET *Phys. Med. Biol.* **66** 195001

Kratochwil N, Gundacker S, Lecoq P and Auffray E 2020 Pushing Cherenkov PET with BGO via coincidence time resolution classification and correction *Phys. Med. Biol.* **65** 115004

Krause P, Rogers E, Birowosuto M D, Pei Q, Auffray E, Vasil'ev A and Bizarri G 2021 Design Rules for Time of Flight Positron Emission Tomography (ToF-PET) Heterostructure Radiation Detectors *SSRN*)

Lecoq P, Konstantinou G, Latella R, Moliner L, Nuyts J, Zhang L, Barrio J, Benlloch J M and Gonzalez A J 2021 Metascintillators: New Results for TOF-PET Applications *IEEE Transactions on Radiation and Plasma Medical Sciences* **6** 510–16

Lecoq P, Morel C, Prior J O, Visvikis D, Gundacker S, Auffray E, Križan P, Turtos R M, Thers D and Charbon E 2020 Roadmap toward the 10 ps time-of-flight PET challenge *Phys. Med. Biol.* **65** 21RM01

Lee M S, Cates J W, Gonzalez-Montoro A and Levin C S 2021 High-resolution time-of-flight PET detector with 100 ps coincidence time resolution using a side-coupled phoswich configuration *Phys. Med. Biol.* **66** 125007

Loignon-Houle F, Charlebois S A, Fontaine R and Lecomte R 2022 Monte Carlo simulations of energy, time and spatial evolution of primary electrons generated by 511 keV photons in various scintillators *Nucl. Instrum. Methods Phys. Res. A* **1030** 166449

Loignon-Houle F, Gundacker S, Toussaint M, Lemyre F C, Auffray E, Fontaine R, Charlebois S A, Lecoq P and Lecomte R 2021 DOI estimation through signal arrival time distribution: a theoretical description including proof of concept measurements *Phys. Med. Biol.* **66** 095015

Lois C, Jakoby B W, Long M J, Hubner K F, Barker D W, Casey M E, Conti M, Panin V Y, Kadrmas D J and Townsend D W 2010 An assessment of the impact of incorporating time-of-flight information into clinical PET/CT imaging *J. Nucl. Med.* **51** 237–45

Mohr P, Efthimiou N, Pagano F, Kratochwil N, Pizzichemi M, Tsoumpas C, Auffray E and Ziemons K 2022 Image Reconstruction Analysis for Positron Emission Tomography with Heterostructured Scintillators *TechRxiv* 10.36227/techrxiv.19929731.v1 01.06.2022 IEEE Trans. Radiat. Plasma Med. Sci.

Moses W W 2003 Time of flight in PET revisited *IEEE Trans. Nucl. Sci.* **50** 1325–30

Moses W W and Derenzo S 1999 Prospects for time-of-flight PET using LSO scintillator *IEEE Trans. Nucl. Sci.* **46** 474–8

Nolet F, Dubois F, Roy N, Parent S, Lemaire W, Massie-Godon A, Charlebois S A, Fontaine R and Pratte J F 2018 Digital SiPM channel integrated in CMOS 65 nm with 17.5 ps FWHM single photon timing resolution *Nucl. Instrum. Methods Phys. Res. A* **912** 29–32

Omelkov S, Nagirnyi V, Vasil A and Kirm M 2016 New features of hot intraband luminescence for fast timing *J. Lumin.* **176** 309–17

Perego J, Villa I, Pedrini A, Padovani E, Crapanzano R, Vedda A, Dujardin C, Bezuidenhout C X, Bracco S and Sozzani P 2021 Composite fast scintillators based on high-Z fluorescent metal–organic framework nanocrystals *Nat. Photonics* **15** 393–400

Pizzichemi M, Polesel A, Stringhini G, Gundacker S, Lecoq P, Tavernier S, Paganoni M and Auffray E 2019 On light sharing TOF-PET modules with depth of interaction and 157 ps FWHM coincidence time resolution *Phys. Med. Biol.* **64** 155008

Pots R, Auffray E and Gundacker S 2020 Exploiting Cross-Luminescence in BaF22 for Ultrafast Timing Applications Using Deep-Ultraviolet Sensitive HPK Silicon Photomultipliers *Front. Phys.* **8** 482

Pourashraf S, Gonzalez-Montoro A, Won J Y, Lee M S, Cates J W, Zhao Z, Lee J S and Levin C S 2021 Scalable electronic readout design for a 100 ps coincidence time resolution TOF-PET system *Phys. Med. Biol.* **66** 085005

Rausch I, Ruiz A, Valverde-Pascual I, Cal-Gonzalez J, Beyer T and Carrio I 2019 Performance Evaluation of the Vereos PET/CT System According to the NEMA NU2-2012 Standard *J. Nucl. Med.* **60** 561–7

Schaart D R 2021 Physics and technology of time-of-flight PET detectors *Phys Med Biol* **66** 09TR01

Surti S, Kuhn A, Werner M E, Perkins A E, Kolthammer J and Karp J S 2007 Performance of Philips Gemini TF PET/CT scanner with special consideration for its time-of-flight imaging capabilities *J. Nucl. Med.* **48** 471–80

Terragni G, Pizzichemi M, Roncali E, Cherry S, Glodo J, Shah K, Arino-Estrada G, Auffray E, Ghezzi A and Kratochwil N 2022 Time Resolution Studies of Thallium Based Cherenkov Semiconductors *Frontiers in Physics* **10** 93

The 10 ps challenge website (https://the10ps-challenge.org)

Toci G, Gizzi L A, Koester P, Baffigi F, Fulgentini L, Labate L, Hospodkova A, Jary V, Nikl M and Vannini M 2019 InGaN/GaN multiple quantum well for superfast scintillation application: Photoluminescence measurements of the picosecond rise time and excitation density effect *J. Lumin.* **208** 119–24

Tomanova K, Čuba V, Brik M G, Mihokova E, Martinez Turtos R, Lecoq P, Auffray E and Nikl M 2019 On the structure, synthesis, and characterization of ultrafast blue-emitting CsPbBr3nanoplatelets *APL Materials* **7** 011104

Turtos R M *et al* 2019a On the use of CdSe scintillating nanoplatelets as time taggers for high-energy gamma detection *npj 2D Mater. Appl.* **3** 1–10

Turtos R M, Gundacker S, Auffray E and Lecoq P 2019b Towards a metamaterial approach for fast timing in PET: experimental proof-of-concept *Phys. Med. Biol.* **64** 185018

Van Sluis J, De Jong J, Schaar J, Noordzij W, Van Snick P, Dierckx R, Borra R, Willemsen A and Boellaard R 2019 Performance Characteristics of the Digital Biograph Vision PET/CT System *J. Nucl. Med.* **60** 1031–6

Vaněček V, Paterek J, Kral R, Kučerkova R, Babin V, Rohliček J, Cala R, Kratochwil N, Auffray E and Nikl M 2021 Ultraviolet cross-luminescence in ternary chlorides of alkali and alkaline-earth metals *Opt. Mater. X* **12** 100103